Needle-Type Image Sensor With Band-Pass Composite Emission Filter and Parallel Fiber-Coupled Laser Excitation

Erus Rustami[ID], *Student Member, IEEE*, Kiyotaka Sasagawa[ID], *Member, IEEE*, Kenji Sugie, Yasumi Ohta, Makito Haruta, Toshihiko Noda, *Member, IEEE*, Takashi Tokuda[ID], *Member, IEEE*, and Jun Ohta[ID], *Senior Member, IEEE*

Abstract—This paper presents an implantable fluorescence system with a composite emission filter and fiber-coupled laser excitation. The composite structure of the short-pass interference filter and absorption filters exhibited a band-pass spectrum between 510 and 570 nm, which is close to green fluorescent protein (GFP) emission. A high-quality excitation light was achieved by utilizing a blue laser through a low-numerical-aperture optical fiber. This coupling method is beneficial in delivering a narrow spectrum and controllable irradiation light in a specific area to minimize auto-fluorescence from the tissue. The fabricated lensless system performance is experimentally validated by imaging emission. The proposed device is capable of perceiving fluorescence emission from microspheres and GFP noticeably.

Index Terms—Implantable imager, lensless imaging, fluorescence, laser-coupling, interference filter.

I. INTRODUCTION

IMPLANTABLE imagers are powerful tools for elucidating the animal brain function owing to their ability of delineating the relation between neural activity and behavior under the free-living condition, which is enabled by features such as wide field of view, lightweight, and low invasiveness [1]–[4]. Various implantable imagers have been developed, so far, by utilizing fluorescence measurements for particular target

detection in different brain areas. For example, the fiber optic fluorescence imaging system based on micro-fabricated components enables highly stable long-term optical imaging and manipulation of neuronal activity in deep brain regions [5], [6] and a multimode fiber can be used for a high-resolution endoscopic application [7]–[9]. Another approach is miniaturized fluorescence microscopy, which integrates micro-optic and semiconductor optoelectronics in a compendious package. This imaging system coincides with mechanical flexibility features as it can be plainly mounted in a rodent's head and inherently conserve high-quality images, resembling the conventional lens-based microscopy [10]–[12]. However, the behavior experiment, which requires intensely freely moving, either optical fiber fluorescence or midget microscopy is too rigid and exorbitant in both size and weight [13].

In an effort of resembling a freely moving condition, a lensless fluorescence system is a favorable imaging modality because of its measly physical embodiments [14]. The absence of optical components in this system has significantly diminished the system. For the implanted device, an inevitable trade-off exists between spatial resolution and invasiveness features. Practically, it is difficult to establish a prover value of the resolution and low invasiveness simultaneously. Therefore, the image sensor is designed according to the variety and area of target detections. The examples include planar-type implanted devices placed on the brain surface for blood observation [15] and hemodynamic response [16], [17]. This implanted version can typically accommodate a broad configuration with several excitation light sources and pixels. In contrast, a needle-type and finer structure are required for devices implanted in the deep brain region, such as for amygdala [13] and optical theranostic applications in a deep tissue [18].

However, the resolution of the existing lensless fluorescence system is much lower than that of the conventional lens-based microscopy. The undirected fluorescence emission, which declines faster as a distance function from the target than its excitation counterpart, leads to low signal-to-background levels. In addition, the fluorescence emission is incoherent, and thus, incompatible for any type of image processing method based on the source-shifting technique, such as holographic digital reconstruction and related super-resolution techniques.
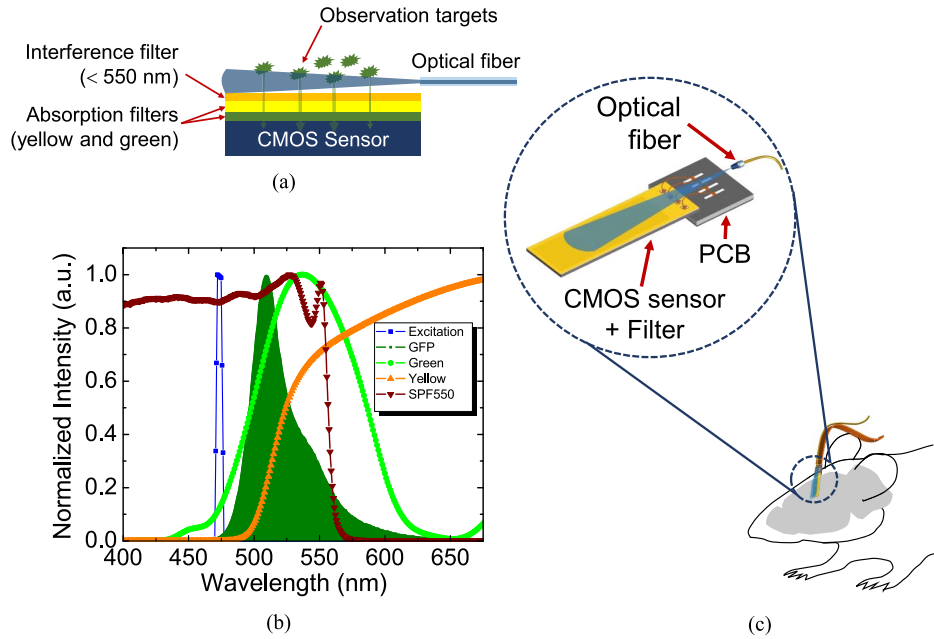
Fig. 1. (a) Structure of a composite filter comprising interference and absorption filters and fiber-coupled laser excitation for target emission detection. (b) Normalized intensity of blue laser excitation light, GFP emission, and interference and absorption filters spectrum. (c) Future application of a needle-type fluorescence imager integrated with fiber-coupled laser for deep brain observation.

In the hardware approach, the insufficient rejection performance of the emission filter contributes to the modest resolution of the lensless system.

A recently developed hybrid emission filter, composed of an interference filter and an absorption filter via a fiber optic plate (FOP), exhibits a high-performance excitation light rejection ratio of approximately 10^8:1 at a wavelength of 450 nm, even in a lensless setup [19], [20]. Notwithstanding this accomplishment, the FOP that is utilized as a substrate for the interference filter, as well as absorption filter-surface protection, has escalated the device thickness into millimeter range. In view of invasiveness, this hybrid filter structure is not suitable for an implantable imaging system, especially for deep brain observation.

This paper proposes a thin composite emission filter, integrated with a fiber-coupled laser, for a high-excitation-rejection fluorescence implantable imager. The sandwich-like structure of the short-pass interference filter, as well as yellow and green absorption filters, exhibits a high-quality band-pass transmission between 510 and 570 nm, which is close to green fluorescent protein (GFP) emission, in an amiable thickness for the implanted device. In addition, laser coupling is beneficial in providing a narrow spectrum and controllable irradiation in a specific area. Moreover, as a remote delivery of the light, the sample temperature increases due to the light source illumination can be suppressed. As a result, the proposed imaging system enables us to perceive the fluorescence emission from microspheres, as well as GFP, in the brain slice noticeably.

The rest of this paper is organized as follows. Section II presents the overview of an implantable imager with a composite emission filter and fiber-coupled laser excitation. Section III describes the device fabrication process, including a multilayer filter-stacking stage, device assembly, and CMOS

image sensor specifications. Section IV presents the filter surface examination, excitation light source characterization, pixel sensitivity, fluorescent microsphere detection for spatial resolution examination, and an *in vitro* experiment using GFP-modified mice brain slice results.

II. IMPLANTABLE IMAGER OVERVIEW

As illustrated in Fig. 1(a), the structure of an implantable imager composed of a CMOS image sensor, multilayer filters, and a fiber-coupled laser. A sandwich-like filter, which is accomplished by directly stacking multilayer filters, plays an important role in preserving the implanted device thickness; meanwhile, the complementary structure of the interference filter and absorption filters enhances the excitation light rejection ratio by generating a composite band-pass transmission close to the GFP emission. This band-pass spectrum resulted from the coalescence absorption and reflection mechanism of all the filters. Fig. 1(b) shows the transmission spectrum of a 550-nm short-pass interference filter (SPF550) and yellow and green absorption filters are relatively close to the GFP emission region. Meanwhile, the narrow spectrum of blue laser excitation light is outside of the detection region.

Fig. 1 (c) shows the future application of fabricated fluorescence implantable devices for brain activity observation. This implanted device is a wire-based type that utilizes the wires for electrical support function and data communication. The electrical wire can be bundled with the optical fiber of excitation light. Practically, only the imaging area, which is represented by an image sensor integrated with a filter, is implanted in the brain. The PCB and optical fiber will be fixed on the cement over the rodent's head.

An interference filter, which is typically formed by the periodical structure of dielectric materials with different refractive
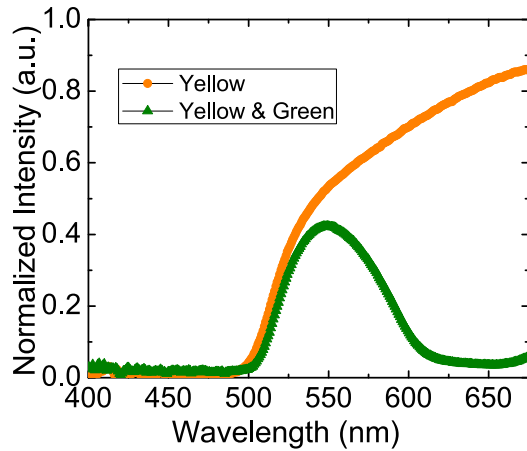
Fig. 2. Transmission spectrum of the yellow and the assembled yellow and green absorption filter.

indices, reflects light in its rejection band so that it is almost free from the auto-fluorescence, as that occurring in the absorption filter. A 550-nm short-pass interference filter reflects red fluorescence from the tissue and passes a GFP emission that is shorter than the interference cut-off region. The interference filter is selected to realize a selective high-quality band-pass transmission spectrum, as its short-pass rejection band can be designed by selecting several dielectric layers. By contrast, it is almost impossible to prepare a short-pass absorption filter with sufficient color selectivity. However, as the interference filter transmission spectrum is angle-dependent, a high-angled fiber-coupled laser and scattered components from the observation targets that are out of its rejection band will pass through the filter. This excitation light infiltration, particularly for targets with both excitation and emission peaks close to each other, such as GFP, will significantly reduce the excitation rejection performance [19].

An absorption filter that resolves this high-angled exci-tation problem as its transmission spectrum is independent of the incident angle of light. For instance, a yellow filter was employed to entirely absorb the blue excitation light. Yet, under the intense excitation light condition, a radiative process frequently occurred and some energy was emitted as fluorescent light out of the absorption band, reducing the observation target emission detection [19], [20]. Consequently, an effective limitation exists while improving the excitation rejection level by increasing the absorption thickness.

Regarding the filter structure, the green absorption filter will absorb a part of auto-fluorescence from the yellow filter and ensures that the emission light that reaches the image sensor comes from GFP. As the green filter transmission spectrum started from 440 nm, the amount of blue excitation light will pass through the filter and reach the image sensor. This infiltration light will alleviate the excitation rejection ratio. Thus, the green and yellow absorption filters are working complementarily to enhance the detection selectivity. Fig. 2. shows the transmission spectrum of the yellow filter and integrated yellow and green filters.

To manage the excitation direction, a blue laser that is coupled on a low-numerical-aperture (NA) optical fiber placed on the edge and almost parallel with the sensor is required. A controllable blue light from the optical fiber minimizes the auto-fluorescence from the tissue due to the abundance of the pigmented substance with an absorption maximum in the blue-green region of the spectrum [21]. In addition, the blue laser narrow spectrum is able to circumvent the undesirable detection of green light which is inherently emitted from a blue light-emitting diode (LED). Furthermore, by assigning the optical fiber parallel to the image sensor makes possible decoupling the illumination and detection of optical pathways; the excitation and emission light travel in a different path through the sample. As a result, this configuration can improve detection selectivity and rejection ratio and avoiding the over-exposure of the sensor because of overwhelming excitation light as well.

III. DEVICE FABRICATION

A. Imaging Device Assembly

Generally, there are two approaches for integrating an emission filter, typically an interference filter, with a CMOS image sensor: on-chip deposition method and transferred filter method. The on-chip deposition method has advantages such as reduced module thickness, the potential for implementation of different filters on pixels, and the elimination of costly exter-nal glass substrates with multiple filters [22], [23]. Conversely, the transferred filter method utilizes a prefabricated interfer-ence filter that is either commercially available or specifically designed by the user. This method is much simpler and cheaper, as the fabrication process is not as complicated as the on-chip deposition, which requires fabrication process adjust-ment to compensate for the material mismatches between the CMOS die and the optical filter [24]. Traditionally, a high-quality interference filter can be fabricated on a firm and stable glass substrate, which is quite difficult to grow in a polymer-based substrate.

Our composite filters were fabricated using the transferred method, combined with a spin-coating technique, for absorp-tion filter deposition prior to the assembly process. The laser lift-off (LLO) method was employed to separate the fabricated filter from its substrate. A commercial 550-nm short-pass interference filter (49-826, Edmund Optics, USA) with an ultraviolet (UV)-grade fused silica substrate, which allows high-energy laser treatment for interference filter separation, was used. The yellow and green dye-based absorption filters were deposited to the interference filter, respectively. First, Valifast Yellow 3150 (Orient Chemical, Japan), cyclopen-tanone (Wako, Japan), and NOA63 (Norland Product, USA) were mixed in a weight ratio of 1:2:1. This mixture was spin-coated onto the interference filter at 1000 rpm, then cured by UV irradiation for 30 s, and finally, heated to 150°C for 45 min. After that, a green absorption filter was directly spin-coated onto the yellow filter layer at 1000 rpm. Finally, this multilayer filter was cured by UV irradiation and heated to 120°C for 2 min and 200°C for 20 min. The fabricated filter was cured at room temperature for 24 h before being used in the assembly process.

1. Attaching the chip
Filter
Image sensor

2. Cutting filter and removing the chip

3. Immobilizing the chip
Epoxy resin

4. Connecting and covering the wires
Epoxy resin
Al wires

5. Coating Parylene film
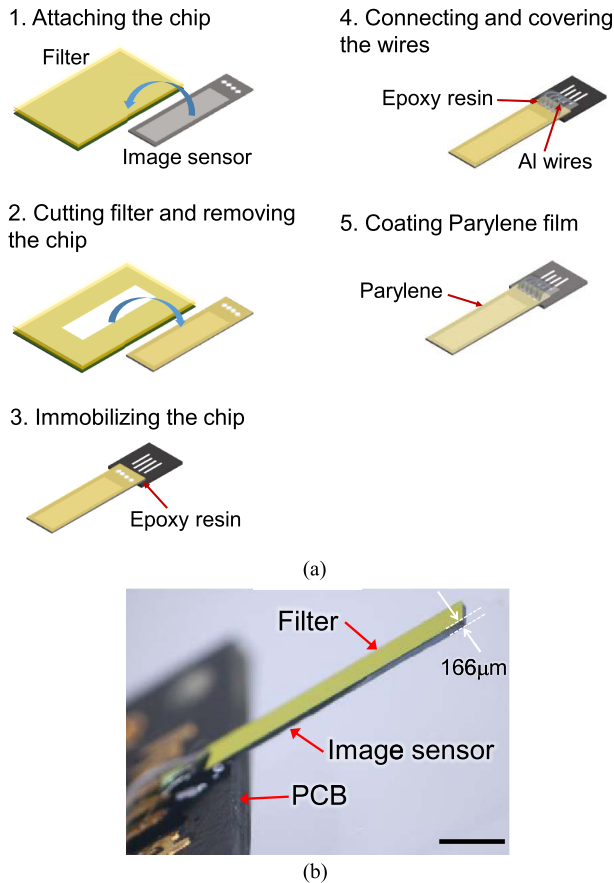Parylene

(a)

Filter
166μm
Image sensor
PCB

(b)

Fig. 3. (a) Fabrication of imaging device started from (1) chip and filter attachment, (2) filter transfer using laser lift-off technique, (3) chip and PCB assembly, (4) electrical wiring, and (5) Parylene coating for sensor protection. (b) Photograph of fabricated image sensor comprises image sensor, composite filter, and PCB. The device thickness is 166 μm and scale bar is 1 mm.

The device assembly process is shown in Fig. 3 (a), and is described as follows:

- A CMOS image sensor chip was fixed onto the filter layers using epoxy resin (Z-1; Nissin resin, Japan) by heating at 120°C for 25 min. The pixel area of the image sensor directly contacted the filter.
- The filter layer was cut by a high-precision laser (Q-switched Nd: YAG laser, $\lambda = 266$ nm) according to the image sensor size. After that, the filter and substrate were separated using the LLO method. This method is traditionally used to separate semiconductor structures such as thin-film GaN from their substrate by utilizing a high-power pulsed laser from the backside of the substrate for selective laser ablation and thermal decomposition of the interfacial layer [25]–[28]. In our fabrication setup, the fourth harmonic pulses of a Q-switched Nd: YAG laser ($\lambda = 266$ nm) irradiated the interfacial area between the fused silica substrates and the interference filters. For a fast and large-yield separation area, rectangular laser fields were stitched using the step-and-repeat technique [29]. After the laser irradiation, the image sensor and filters were manually removed from the substrate. For

the electrical wiring connection, the filter at the chip pad region then removed by a low-energy Nd: YAG laser.
- Next, a fabricated device was bonded on the designated printed circuit board (PCB) using epoxy resin (Z-1; Nissin resin, Japan) by heating at 120°C for 30 min for immobilization.
- The electrical bonding pads of the CMOS image sensor were connected to the PCB via aluminum (Al) wires using a wire bonder (7700CP, West Bond Inc., Anaheim, CA, USA). Then, epoxy resin (Z-1; Nissin resin, Japan) was added to the wires and heated at 120°C for 25 min for wire protection.
- For waterproofing and biocompatibility features, the imaging device was coated with a Parylene-C film using a Parylene coating chamber (PDS2010 Specialty Coating Systems, NIST, USA).

The fabricated device thickness, as shown in Fig. 3 (b), is 166 μm whereby the CMOS sensor and composite filter thickness are 150 μm and 16 μm, respectively. This thickness level is acceptable to measure the fluorescence emission in the deep brain region as it is thin enough to limit damage to surrounding tissue as it is inserted in the brain [13]. However, in a practical application, increasing device thickness due to the presence of optical fiber should be considered. For instance, it will append about 100 μm for a multimode optical fiber, which will literally escalate the damage of the brain during the insertion process. One way to resolve this thickness issue is by utilizing an on-chip waveguide instead of a bulky-optical fiber for delivering the excitation light. This fine waveguide thickness can be flexibly designed according to the light intensity requirement. Yet, the implementation of the on-chip waveguide on the fluorescence imager is beyond the scope of this article. The total weight of the fabricated device, including PCB, is about 0.05 g.

B. CMOS Image Sensor Circuitry

A needle-type image sensor, which contains 40 × 400 pixels, was designed in our lab and fabricated by the foundry using 0.35-μm 2-poly 4-metal standard CMOS technology (AMS). The chip dimensions include a width of 500 μm, length of 5100 μm, and thickness of 150 μm.

Fig. 4 (a) depicts the schematic circuit of a needle CMOS sensor. It consists of 40 × 400 active pixel array, control circuitry for selecting the pixels via a Y-scanner (row) at the left-side and column amplifier and X-scanner at the bottom of the pixel array. Bias circuit and power-on-reset are supporting circuitry for the imaging process.

For the imaging function, a pixel array with a size of 7.5 μm × 7.5 μm/pixels was selected to provide sufficient spatial resolution for imaging the colony of the brain neural cell. This pixel uses a three-transistor active pixel sensor (3-Tr APS) for transducing the optical to an electrical voltage. As can be seen in the pixel sensor schematic, 3-Tr APS consists of a photodetector and three transistors for switching and a source follower.

The operation of an APS as follows. At the beginning of detection, the photodiode (PD) is reset by sending the Y_{RST}
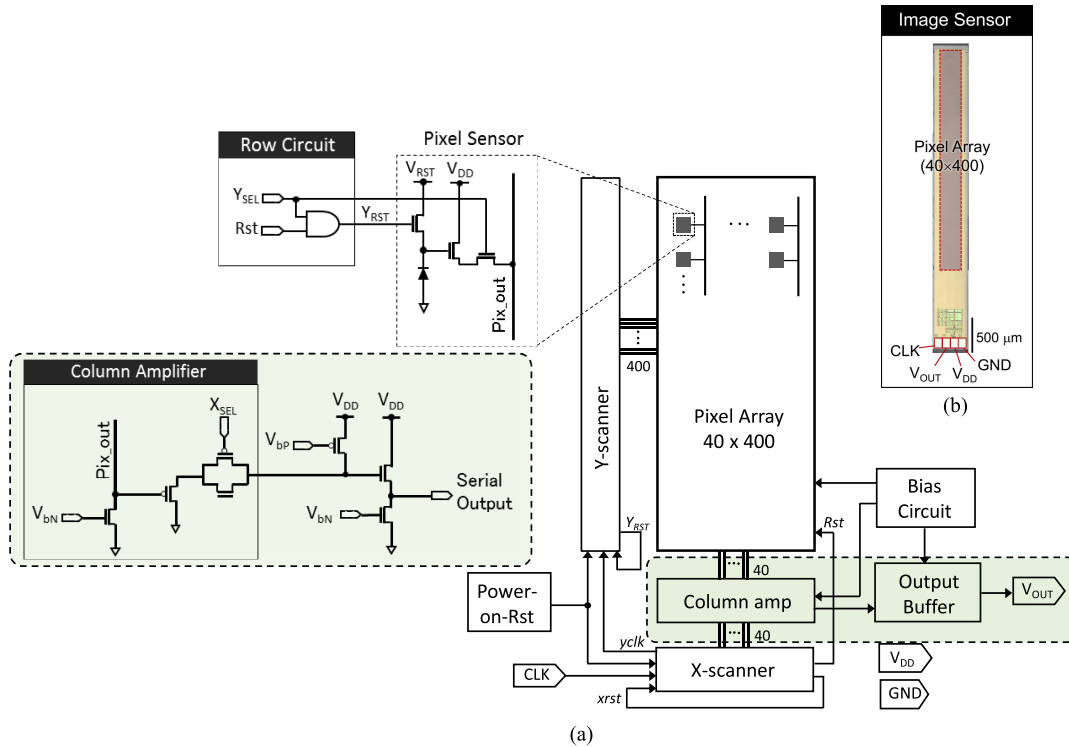
Fig. 4. (a) Schematic diagram of the needle-type CMOS image sensor that consists of pixel array based on three-transistor active pixel sensor (3-Tr APS) structure, Y-scanner for row selectivity, column amplifier and output buffer circuit, and X-scanner for column addressing. (b) Microphotograph of the CMOS needle sensor with the four pads connector (V_{DD}, GND, CLK, and V_{OUT}).

command activating the switch. This action forced the PD to a specific voltage level. Next, the integration period started by turned off the Y_{RST} transistor, which makes PD is electrically floated. During this period, the incident light produces carriers and accumulated in the PD junction capacitance; the voltage of PD decreases proportionally to the input light intensity. The total amount of the incident light can be obtained by measuring the voltage drop. After an accumulation time, the Y_{SEL} turned on the switch and then transferred the PD levels of selected pixels to be read out in the vertical output line, *Pix_out*. After the voltage reading process is finished, the Y_{RST} is turned off and repeat a similar process for the next pixel.

The operational sequence of the pixel selectivity relies on the Y-scanner for selecting the light-sensing rows one-by-one. Every pixel in the selected rows is connected to the column circuitry, which comprises the source follower circuit and column selecting transistor switch, X_{SEL}, via each column signal line. The column amplifier output is then connected to the buffer circuit for signal maintaining, before sending it out to the next data processing stage. For this data communication and electrical function, the image sensor has four pads connectors, V_{DD}, GND, CLK, and V_{OUT} as can be seen in Fig. 4 (b). The image sensor specifications are shown in Table I.

IV. RESULTS

A. Filter Surface Examination

We investigated surface morphologies and optical properties of the interference filter after the lift-off process. The surface filter profiling is important for determining laser ablation

TABLE I
SPECIFICATIONS OF THE IMAGE SENSOR

Process technology	0.35-μm 2-poly 4-metal standard CMOS process
Supply voltage (V)	3.3
Chip size (μm²)	500×5100
Pixel type	3-transistor active pixel sensor
Pixel size (μm²)	7.5×7.5
Pixel array size	40×400
Photodiode type	Nwell-Psub

effects on the interference filter structure. As the high-intensity laser beam hits the interface area between the substrate and the filter, its temperature rises and at some level it will force the material to undergo a phase change from the solid to gaseous state. This phase transition results in a mass loss from the lowermost layer. The decreasing number of layers in the interference filter structure may predispose its optical properties.

Fig. 5 (a) shows the difference in height of the irradiated filter captured by a surface profiler (ET200, Kosaka Laboratory, Japan). As can be seen, the inhomogeneous surface varies about $\pm$ 0.02 μm from its initial position. This number is closely associated with a single-layer thickness, which means the laser ablation of the lift-off process has eradicated a single layer, yet did not affect another layer. Furthermore, we compared the transmission spectrum of the interference
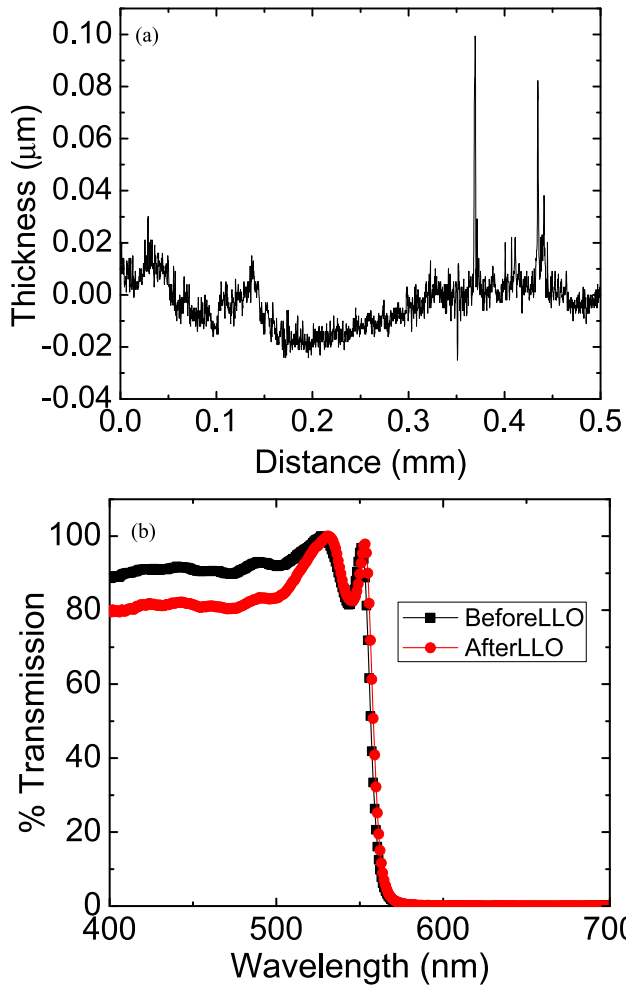
Fig. 5. (a) Interference filter surface roughness profile after LLO. (b) Transmission spectrum comparison of interference filter before and after LLO.
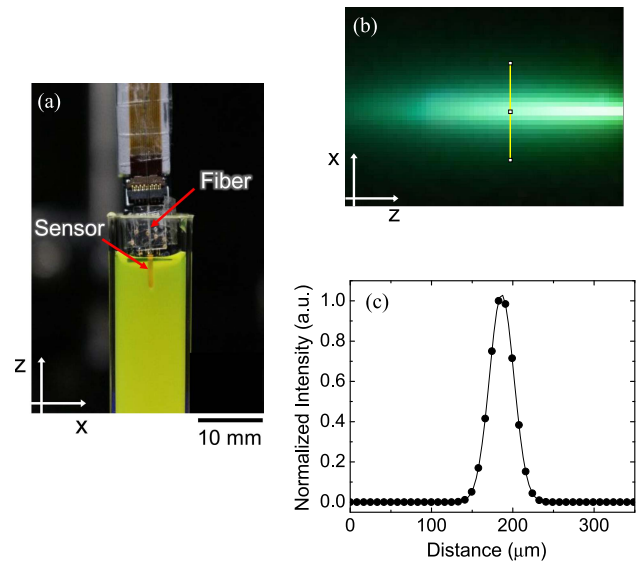

Fig. 6. (a) Photograph of fiber-coupled laser assembled with the image sensor in the Uranine-filled glass cuvette. (b) Lateral views for the light-sheet thickness. (c) Light intensity profile alongside the yellow line at the light profile (b) that is fitted with the Gaussian distribution.
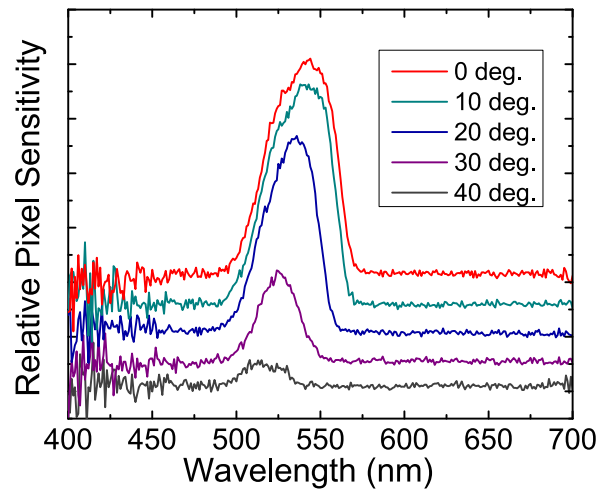

Fig. 7. Pixel sensitivity spectrum of an image sensor integrated with the composite filter at various incident angles of the excitation light. The baseline are shifted to improve readability.

filter before and after the lift-off process. As can be seen in Fig. 5 (b), both filters show similar transmission patterns. This means, as the interference has many periodical layers, diminishing a single layer does not change the operational rejection band. The percentage of transmission after lift-off is lower about 10 % than that of the initial filter, which may contribute to reflection performance deterioration.

B. Laser Profile Characterization

Fig. 6 (a) shows the fiber-coupled laser profile examination setup, which the assembled optical fiber and an image sensor was immersed in 100 μM of Uranine-filled glass cuvette. The tapered optical fiber was placed onto PCB on the topside of the cuvette. A blue laser ($\lambda = 473$ nm) illuminated the samples and generated an observable light path as can be seen in Fig. 6 (b).

The low-NA multimode optical fiber ($\varphi_{\text{core}} = 25$ μm, NA $= 0.1$) delivers a narrow beam along the image sensor area. As we utilized a commercialized laser beam without any optical treatment, the laser intensity did not uniformly propagate throughout the imaging areas. The intensity profile as denoted with the yellow line was measured to obtain

the spatial distribution of laser excitation. Fig. 6 (c) shows the light intensity fitted with Gaussian distribution and the full half-width maximum (FWHM) is 35.52 μm. With this spatial distribution profile, the disperse observation targets (i.e GFP) will receive different excitation light intensity and then produce unequal fluorescence emission levels. In addition, as the laser beam could not cover the pixel areas entirely, it is difficult to perceive all the emission in a single-mode detection. To resolve this drawback, image processing can be used to concatenate images from different light source positions.

C. Pixel Sensitivity Characteristic

The composite filter response of incident light was examined by pixel sensitivity measurement. The fabricated device

integrated with a composite filter was irradiated with a light source ranging from 400 to 675 nm (MicroHR Spectrometer, Horiba, Japan). To imitate the light path that comes to the image sensor in the real applications, which contains many scattering components, we did not use an objective lens instead of employing an optical aperture for shaping the light source beam. We measured the pixel sensitivity spectrum of the fabricated device at a normal incident angle, which is the optimum angle for the interference filter to operate in its rejection band. However, in the brain observation experiment, incident light does not always come from this normal angle; Mostly, the light travels in a random path with a different angle. Therefore, we varied the incidence angle of excitation light to examine the transmission spectrum of fabricated composite filters.

As shown in Fig. 7, particularly in a normal incident angle, the composite filter exhibited a band-pass transmission spectrum in the range 510–570 nm, which is relatively associated with GFP emission, and all lights out of the transmission band were significantly reduced. This band-pass transmission profile is a result of a complement filter mechanism. A wavelength longer than 570 nm was reflected by the short-pass interference filter, whereas a light shorter than 510 nm was absorbed by the yellow and green absorption filter. From this band-pass transmission profile, the composite filter is intended to suppress auto-fluorescence from the tissue.

The interference filter spectrum shifted to a shorter wavelength by increasing the incident angle, while the absorption filter spectrum is fixed for all incident angles. Thus, the transmission band is narrowed by an increase in the incident angle and leads to a lower sensitivity profile. In addition, the incident angle inclination results in sensitivity degradation. This effect reduces the effective NA of the sensor, and thus, the resolution degradation ratio with the distance is decreased.

The interference filter has a rejection band. Light with a wavelength longer than the rejection band edge of the short-pass filter is reflected. Due to the spectrum shift with an incident angle, the highly tilted excitation light and the auto-fluorescence from the tissue are transmitted. However, in the proposed filter, these components are reduced by the yellow and green absorption filters. The thin absorption filters work well for low-incident-angle light.

We confirmed that the transmission shifting of the interference filter due to the incidence angle variation will not affect the composite filter bandwidth characteristic. The filter transmission spectrum operates close to the GPF region in all angle variation. In the proposed device the optical fiber was placed parallel to the image sensor so that the direct excitation light on the image sensor can be sufficiently rejected.

D. Fluorescent Image From Microspheres

We first verified the fluorescence detection capability of our device using imaging fluorescent microspheres. We observed emission from green-yellow fluorescent microspheres of 15-μm diameter (F8844, ThermoFisher Scientific, Massachusetts, US), for mimicking fluorescently labeled cells. The excitation and emission peaks of the microspheres were 505 and 515 nm, respectively. These microspheres were double
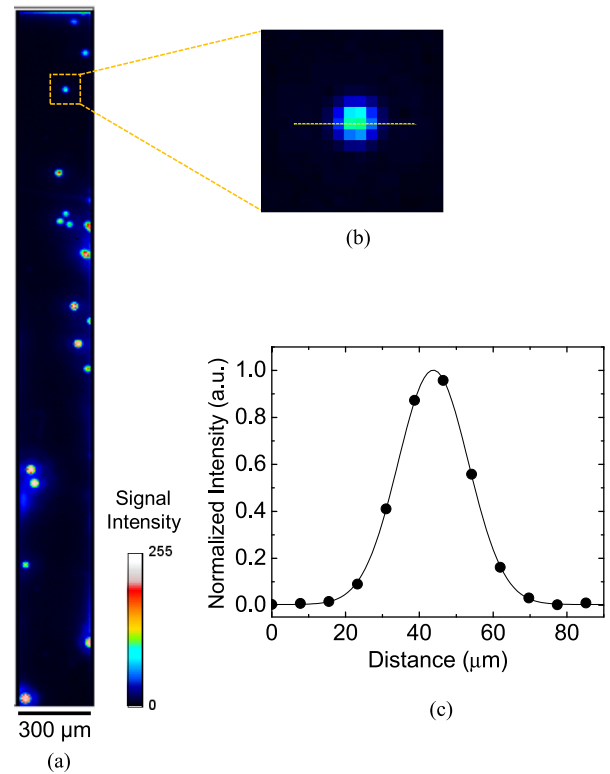

Fig. 8. Fluorescence imaging performance of fabricated imaging sensor with the composite filter. (a) Fluorescent image obtained from yellow-green microsphere with blue laser excitation light ($\lambda = 473$ nm). (b) ROI image of unsaturated emission for image sensor resolution examination. (c) Intensity profile alongside the yellow line of (b) of microspheres. The experimental data are fitted with the Gaussian function.

the pixel size used in the device and directly contacted the image sensor surface to avoid resolution degradation.

The fluorescence imaging of the fabricated device was performed with a fiber-coupled blue laser ($\lambda = 473$ nm) placed at the edge and almost parallel with the image sensor on the opposite side of PCB. Due to the presence of wire connection from PCB to image sensor, it was difficult getting the almost perfectly parallel illumination if the fiber was placed on the PCB side. This new setup will not much affect the filter selectivity as discussed in subsection IV.C. The position of excitation light was fixed during the microsphere emission observation. The laser power measured by an optical power meter (PM100USB, Thorlabs, USA) was 100 μW/cm^2.

As shown in Fig. 8(a), the fluorescent microsphere ($\varphi = 15$ μm) emission was clearly observed in different intensity profiles, which can be classified into saturated and unsaturated profiles. This classification is due to the relative position of microspheres to the excitation light. Some of the beads received more intensity than other beads and become saturated. This saturated bead produces larger shapes than its real dimension because of the overwhelming emission, which will lead to inaccuracy for the spatial resolution measurement.

A region of interest (ROI), of around 125 μm $\times$ 125 μm dimensions, was selected from the single and unsaturated emission, as denoted with a dashed rectangle in Fig. 8 (a). Fig. 8(b) and Fig. 8 (c) shows, respectively, the ROI region

with a yellow line alongside the x-pixels and the intensity profile of the fluorescent microsphere fitted with the Gaussian function.

To clarify the spatial resolution, the FWHM was calculated as 22. 3 μm $\pm$ 1.21 μm. The discrepancy profile of the microsphere emission from its actual dimension was due to the emission filter thickness, which increased the distance between the fluorescent microspheres and the image sensor so that the emission light spreads over the filter and then degrades the resolution. Nevertheless, the resolution of the fabricated devices is still acceptable for brain activity observation [30]. One way to improve the spatial resolution of the implantable device is by utilizing the incident-angle-selective pixel technique. In this technique, pixels, which normal and angle-selective, detect different incident angles via the designed metal aperture structure. As a result, the image reconstruction process can acquire a spatial resolution close to the pixel pitch [31].

E. In Vitro Experiment

Once the responsivity of fluorescence emission was observed, an *in vitro* experiment was performed to confirm the detection performance in biological samples. We used 100-μm-thick brain slices obtained from an adult mouse (GAD67), which was genetically modified by GFP. All procedures for preparing the animal tissue were carried out in accordance with the guidelines of the Nara Institute of Science and Technology. The brain slice was directly placed onto the surface of the image sensor, while the edge of the optical fiber was inserted between the samples and image sensor.

In this experiment, we used an identical light source setting with the microsphere experiment ($P_{optical}$ = 100 μW/cm^2) whereas the optical light source and placed the fiber at the edge of the imaging area. The positions of both the fiber and the image sensor can be controlled manually to deliver the excitation light at the specific area of the samples, and simultaneously, image sensor position adjustment can be performed for obtaining the best imaging result. In addition, as the laser beam could not reach the entire imaging area at one irradiation position, a different light source position can be tailored to obtain a larger area of detection by employing image processing.

This setup is intended to deliver the light source almost parallel to the image sensor. When we utilized the taper for holding the optical fiber on the PCB's side, it was difficult to get a parallel illumination for the very thin brain slice sample due to the presence of wire connection. Therefore, the optical fiber position was moved to another image sensor's edge, which is on the opposite side of the PCB (Fig. 9 (a)). Both of the excitation light and the image sensor positions were controlled by the vertical movement of the optical fiber holder. The small difference in height of the optical fiber and the image sensor produces a various incident angle of the excitation light path through the brain tissue. Tough this fiber-coupled laser arrangement is obviously difficult for implantable device applications as it needs more space and treatment. Yet, the advanced techniques in an on-chip
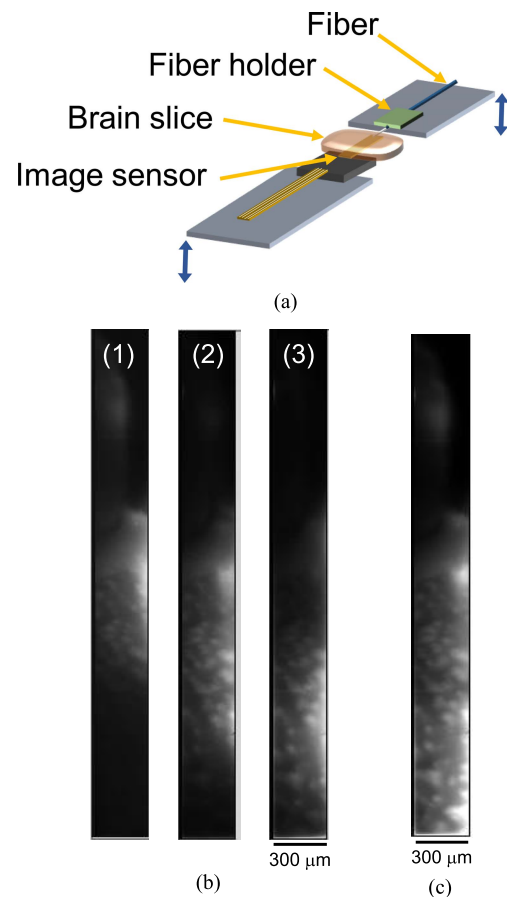

Fig. 9. (a) The experiment setup for fluorescence emission detection with various optical fiber position (b) Fluorescent images obtained by the image sensor. The light source travel from the bottom side. Three different light source position: (1) the furthermost irradiation area, (2) the middle irradiation area, (3) the closest irradiation area. (c) Processed image of different excitation light position for a larger detection area.

waveguide are apparently able to resolve the parallel-excitation light irradiation problem with a very low invasiveness feature.

Fig. 9 (b) shows the fluorescent images obtained using the fabricated devices at three light source positions by changing the angle of the fiber position. The excitation light travels from the bottom side of the images. In the first position (image 1), the optical fiber is almost parallel to the image sensor so that the laser beam irradiated the farthermost area of the brain slice. Then, increasing the angle beam by tailoring the optical fiber position leads to irradiated area displacement; it becomes closer to the light source (images 2 and 3, respectively). This finite detection area comes from the non-uniform laser beam profile and the gap between the brain slice and image sensor due to the optical fiber thickness. However, all the fluorescent images show that the fabricated device can perceive several identical bright areas, which are identified as GFP emission noticeably. The opacity areas observed for each image were due to the excitation light limitation in both intensity and direction, incorporated with scattering and absorption by the brain tissue. Therefore, some areas did not get enough irradiation to generate an observable emission. As predicted, the direct contact between the image sensor and the brain slice improved the spatial resolution imaging.
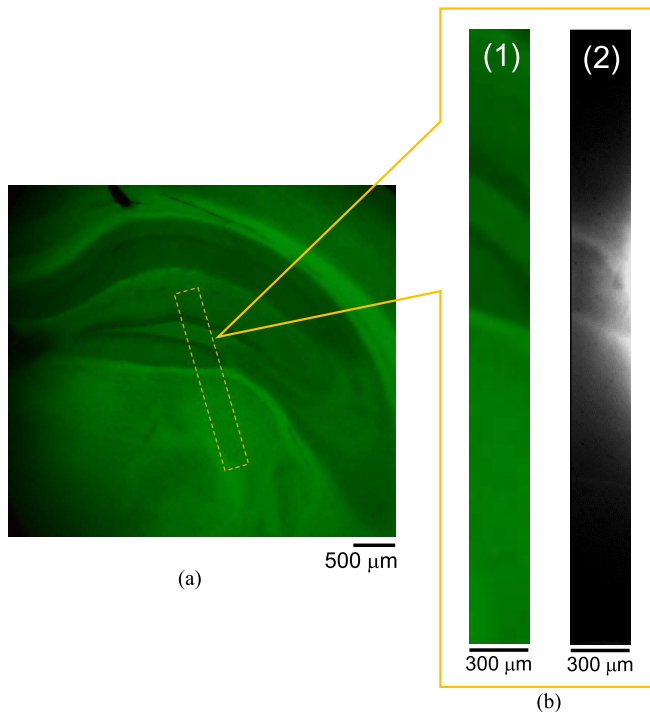
high-spatial-resolution fluorescence imaging. The fabricated device demonstrated the capability of capturing fluorescence emission from the microspheres, as well as GFP, in the brain slice. We expect this method to open up an entirely high-quality fluorescence imaging application with implantable imagers.

Fig. 10. (a) The florescent image of the hippocampus area captured by the fluorescence microscopy. (b) The comparison image of specific area in the hippocampus, denoted by the yellow dashed rectangle at the (a), produced by: (1) lens-based fluorescence microscopy, (2) fabricated device.

To overcome the excitation light coverage limitation and expand the detection area, the image processing technique was employed by combining images from different fiber positions. Then, a little contrast adjustment was applied to improve the image quality. Image processing was performed using MATLAB (2018a, Mathworks, MA, USA); its result is shown in Fig. 9 (c). From this image, the bright areas occupied more than half of the image sensor area. In addition, it can be clearly seen that the observed fluorescence emission patterns are identical and did not change with the incident angle of excitation light variation. Thus, it can be stated that the observable pattern is the emission from GFP.

Fig. 10 (a) shows the hippocampus area captured by lens-based fluorescence microscopy (BX51W1, Olympus, Japan). The target detection area was indicated with a yellow dashed rectangle. The detection comparison of the brain slice between the fabricated device and lens-based fluorescence microscopy can be seen in Fig. 10 (b), whereas the fluorescent image obtained using the fabricated device (image 2) can observe a similar pattern with the lower resolution compared to fluorescence microscopy (image 1). In addition, some saturated emission was observed close to the side of the device. This saturated pixel resulted from the high intensity of the excitation light and might originate from the leakage light caused by filter defects at the side of the images sensor. This shortcoming can be reduced by controlling the excitation light intensity and applying the black resist on the entire side of the image sensor.

V. CONCLUSIONS

We proposed a new method for stacking composite multi-layer filters, combined with fiber-coupled laser excitation, for

REFERENCES

[1] J. Ohta, "Implantable CMOS biomedical devices," *Sensors*, vol. 9, no. 11, pp. 9073–9093, 2009.
[2] D. C. Ng *et al.*, "An implantable and fully integrated complementary metal-oxide semiconductor device for *in vivo* neural imaging and electrical interfacing with the mouse hippocampus," *Sens. Actuators, A Phys.*, vols. 145–146, nos. 1–2, pp. 176–186, Jul. 2008.
[3] D. C. Ng *et al.*, "Real time *in vivo* imaging and measurement of serine protease activity in the mouse hippocampus using a dedicated complementary metal-oxide semiconductor imaging device," *J. Neurosci. Methods*, vol. 156, nos. 1–2, pp. 23–30, Sep. 2006.
[4] T. Kobayashi *et al.*, "Functional neuroimaging by using an implantable CMOS multimodal device in a freely-moving mouse," in *Proc. IEEE Biomed. Circuits Syst. Conf. (BioCAS)*, Nov. 2011, pp. 110–113.
[5] L. V. Doronina-Amitonova *et al.*, "Implantable fiber-optic interface for parallel multisite long-term optical dynamic brain interrogation in freely moving mice," *Sci. Rep.*, vol. 3, Nov. 2013, Art. no. 3265.
[6] D. Miyamoto and M. Murayama, "The fiber-optic imaging and manipulation of neural activity during animal behavior," *Neurosci. Res.*, vol. 103, pp. 1–9, Sep. 2016.
[7] G. Oh, E. Chung, and S. H. Yun, "Optical fibers for high-resolution *in vivo* microendoscopic fluorescence imaging," *Opt. Fiber Technol.*, vol. 19, no. 6, pp. 760–771, Dec. 2013.
[8] S. Turtaev, I. T. Leite, T. Altwegg-Boussac, J. M. P. Pakan, N. L. Rochefort, and T. Čižmár, "High-fidelity multimode fibre-based endoscopy for deep brain *in vivo* imaging," *Light Sci. Appl.*, vol. 7, Nov. 2018, Art. no. 92.
[9] I. N. Papadopoulos, S. Farahi, C. Moser, and D. Psaltis, "High-resolution, lensless endoscope based on digital scanning through a multimode optical fiber," *Biomed. Opt. Express*, vol. 4, no. 2, pp. 260–273, 2013.
[10] J. H. Park *et al.*, "Head-mountable high speed camera for optical neural recording," *J. Neurosci. Methods*, vol. 201, no. 2, pp. 290–295, 2011.
[11] K. K. Ghosh *et al.*, "Miniaturized integration of a fluorescence microscope," *Nature Methods*, vol. 8, no. 10, pp. 871–878, Sep. 2011.
[12] *UCLA Miniscope*. Accessed: Oct. 23, 2018. [Online]. Available: http://miniscope.org/index.php/Main_Page
[13] J. Ohta *et al.*, "Implantable microimaging device for observing brain activities of rodents," *Proc. IEEE*, vol. 105, no. 1, pp. 158–166, Jan. 2017.
[14] A. Ozcan and E. McLeod, "Lensless imaging and sensing," *Annu. Rev. Biomed. Eng.*, vol. 18, no. 1, pp. 77–102, Jul. 2016.
[15] M. Haruta *et al.*, "An implantable CMOS device for blood-flow imaging during experiments on freely moving rats," *Jpn. J. Appl. Phys.*, vol. 53, no. 4S, Apr. 2014, Art. no. 04EL05.
[16] K. Sasagawa *et al.*, "An implantable CMOS image sensor with self-reset pixels for functional brain imaging," *IEEE Trans. Electron Devices*, vol. 63, no. 1, pp. 215–222, Jan. 2016.
[17] T. Yamaguchi *et al.*, "Implantable self-reset CMOS image sensor and its application to hemodynamic response detection in living mouse brain," *Jpn. J. Appl. Phys.*, vol. 55, no. 4S, Apr. 2016, Art. no. 04EM02.
[18] H. Takehara *et al.*, "Implantable micro-optical semiconductor devices for optical theranostics in deep tissue," *Appl. Phys. Express*, vol. 9, no. 4, Mar. 2016, Art. no. 47001.
[19] K. Sasagawa, A. Kimura, M. Haruta, T. Noda, T. Tokuda, and J. Ohta, "Highly sensitive lens-free fluorescence imaging device enabled by a complementary combination of interference and absorption filters," *Biomed. Opt. Express*, vol. 9, no. 9, pp. 4329–4344, 2018.
[20] K. Sasagawa, Y. Ohta, M. Kawahara, M. Haruta, T. Tokuda, and J. Ohta, "Wide field-of-view lensless fluorescence imaging device with hybrid bandpass emission filter," *AIP Adv.*, vol. 9, no. 3, 2019, Art. no. 035108.
[21] H. M. Lai, W. L. Ng, S. M. Gentleman, and W. Wu, "Chemical probes for visualizing intact animal and human brain tissue," *Cell Chem. Biol.*, vol. 24, no. 6, pp. 659–672, 2017.
[22] D. E. Schwartz, P. Gong, and K. L. Shepard, "Time-resolved Förster-resonance-energy-transfer DNA assay on an active CMOS microarray," *Biosens. Bioelectron.*, vol. 24, no. 3, pp. 383–390, 2008.

[23] L. Frey *et al.*, "On-chip copper-dielectric interference filters for manufacturing of ambient light and proximity CMOS sensors," *Appl. Opt.*, vol. 53, no. 20, pp. 4493–4502, 2014.

[24] R. Singh, D. Ho, A. Nilchi, G. Gulak, P. Yau, and R. Genov, "A CMOS/thin-film fluorescence contact imaging microsystem for DNA analysis," *IEEE Trans. Circuits Syst. I, Reg. Papers*, vol. 57, no. 5, pp. 1029–1038, May 2010.

[25] A. Kawan, S.-J. Yu, and J.-H. Sung, "Study of laser lift-off process for fabrication of GaN-based 365-nm ultraviolet absorption layer removed flip chip LED," *Trans. Electr. Electron. Mater.*, vol. 19, no. 3, pp. 230–234, Jun. 2018.

[26] T. Ueda, M. Ishida, and M. Yuri, "Separation of thin GaN from sapphire by laser lift-off technique," *Jpn. J. Appl. Phys.*, vol. 50, no. 4R, Apr. 2011, Art. no. 041001.

[27] W. S. Wong, T. Sands, and N. W. Cheung, "Damage-free separation of GaN thin films from sapphire substrates," *Appl. Phys. Lett.*, vol. 72, no. 5, pp. 599–601, 1998.

[28] W. S. Wong *et al.*, "Fabrication of thin-film InGaN light-emitting diode membranes by laser lift-off," *Appl. Phys. Lett.*, vol. 75, no. 10, pp. 1360–1362, 1999.

[29] R. Delmdahl, R. Pätzel, and J. Brune, "Large-area laser-lift-off processing in microelectronics," *Phys. Procedia*, vol. 41, pp. 241–248, Apr. 2013.

[30] H. Takehara *et al.*, "Intravital fluorescence imaging of mouse brain using implantable semiconductor devices and epi-illumination of biological tissue," *Biomed. Opt. Express*, vol. 6, no. 5, pp. 1553–1564, 2015.

[31] K. Sugie, K. Sasagawa, M. C. Guinto, M. Haruta, T. Tokuda, and J. Ohta, "Implantable CMOS image sensor with incident-angle-selective pixels," *Electron. Lett.*, vol. 55, no. 13, pp. 729–731, 2019.

Erus Rustami (S'19) received the B.S. degree in physics and the M.Sc. degree in biophysics from IPB University, Indonesia, in 2008 and 2012, respectively. He is currently pursuing the Ph.D. degree with the Nara Institute of Science and Technology, Japan.

In 2014, he joined the Department of Physics, IPB University, as a Lecturer. His research interest includes CMOS implantable imager and bioinstrumentation.
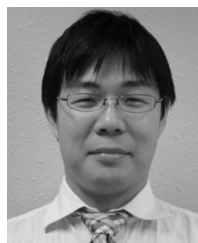
Kiyotaka Sasagawa (M'08) received the B.S. degree from Kyoto University, Kyoto, Japan, in 1999, and the M.E. and Ph.D. degrees in materials science from the Nara Institute of Science and Technology, Nara, Japan, in 2001 and 2004, respectively. From 2004 to 2008, he was a Researcher with the National Institute of Information and Communications Technology, Tokyo, Japan. In 2008, he joined the Nara Institute of Science and Technology, Nara, as an Assistant Professor, where he has been an Associate Professor since 2019. His research interests involve bioimaging, biosensing, and electromagnetic field imaging.
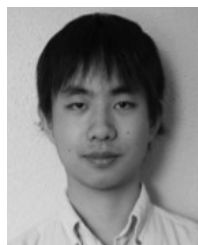
Kenji Sugie received the B.S. degree in electrical and electronic engineering from the University of Ritsumeikan, Kusatsu, Japan. He is currently pursuing the M.S. degree with the Nara Institute of Science and Technology, Nara, Japan. His research interest includes implantable CMOS image sensors for neural activity observation.

Yasumi Ohta received the Ph.D. degree in biophysics science from Kyoto University, Kyoto, Japan, in 2011. In 2011, she joined the Nara Institute of Science and Technology, Japan, as a Post-Doctoral Fellow. Her research interest involves implantable bio-imaging.

Makito Haruta received the B.E. degree in bioscience and biotechnology from Okayama University, Okayama, Japan, in 2009, and the M.S. degree in biological science and the Dr.Eng. degree in material science from the Nara Institute of Science and Technology (NAIST), Nara, Japan, in 2011 and 2014, respectively. He was a Post-Doctoral Fellow with NAIST from 2014 to 2016. He joined the Institute for Research Initiatives, NAIST, in 2016, as an Assistant Professor. In 2019, he joined the Graduate School of Science and Technology, NAIST, as an Assistant Professor. His research interests include brain imaging devices for understanding brain functions related to animal behaviors.

Toshihiko Noda (M'15) received the B.E. and M.E. degrees in electrical and electronic engineering and the Ph.D. degree in engineering from the Toyohashi University of Technology (TUT), Toyohashi, Japan, in 2001, 2003, and 2006, respectively. He was a Post-Doctoral Researcher and an Assistant Professor at TUT from 2006 to 2008. Since 2009, he has been an Assistant Professor at the Nara Institute of Science and Technology (NAIST), Nara, Japan. In 2018, he joined the Faculty of the Electronics-Inspired Interdisciplinary Research Institute (EIIRIS), TUT, as an Associate Professor. His current research focus is on multimodal sensing systems based on CMOS technology.

Takashi Tokuda (M'08) received the B.E. and M.E. degrees in electronic engineering and the Ph.D. degree in materials engineering from Kyoto University, Kyoto, Japan, in 1993, 1995, and 1998, respectively. From 1999 to 2008 and from 2008 to 2019, he was an Assistant Professor with the Graduate School of Materials Science, and Nara Institute of Science and Technology (NAIST), respectively. Since 2019, he has been a Professor at the Tokyo Institute of Technology. His research interests include CMOS image sensors, implantable devices, wireless technology, and IoT.

Jun Ohta (M'97–SM'15) received the B.E., M.E., and Dr.Eng. degrees in applied physics from The University of Tokyo, Japan, in 1981, 1983, and 1992, respectively.

In 1983, he joined Mitsubishi Electric Corporation, Japan. From 1992 to 1993, he was a Visiting Scientist with the Optoelectronics Computing Systems Center, University of Colorado at Boulder. In 1998, he joined the Graduate School of Materials Science, Nara Institute of Science and Technology (NAIST), Nara, Japan, as an Associate Professor. He was appointed as a Professor in 2004. His current research interests include smart CMOS image sensors for biomedical applications and retinal prosthetic devices. He serves as an Associate Editor of the IEEE TRANSACTIONS ON BIOMEDICAL CIRCUITS AND SYSTEMS and an Editorial Board of *Journal of Engineering*, IET. He is a Fellow of the Japan Society of Applied Physics and the Institute of Image, Information, and Television Engineers.